Assessment of Martian dust lifting schemes in the MarsWRF model

[1]Lulu Li, [1,2]Chun Zhao*, [1]Tao Li, [1]Xianghui Xue, [3]Jing Xiao, [4]Zhaopeng Wu, [1]Shengfu Lin, [1]Jiamin Xu, [1]Yongxuan Zhao, [1]Chengyun Yang

[1]Deep Space Exploration Laboratory / School of Earth and Space Sciences, University of Science and Technology of China, Hefei 230026, China

[2]CAS Center for Excellence in Comparative Planetology, University of Science and Technology of China, Hefei, China

[3]Space Science Institute / Lunar and Planetary Science Laboratory, Macau University of Science and Technology, Macau, China

[4]Institute of Geology and Geophysics / Key Laboratory of Earth and Planetary Physics, Chinese Academy of Science, Beijing, China

The manuscript for submission to *JGR-Planets*

*Corresponding author: Chun Zhao (chunzhao@ustc.edu.cn)

Three key points:

1. Current convective lifting scheme can reproduce seasonal variation of global mean dust but not observed spatial distribution of dust devils.
2. There is a discrepancy in the assessment of modeling seasonal variations of dust with T15 and CDOD with current wind stress lifting scheme.
3. Modeling biases in dust spatial distributions may be caused by the biases in lifting processes and large-scale atmospheric circulation.

Abstract

MarsWRF, the general circulation model of Mars, is one of the most commonly used models to study the dust cycle in the Martian atmosphere. It has been widely used to study the mechanisms of dust storms and their effects on the Martian atmosphere. To better understand the ability of MarsWRF to simulate the dust cycle on Mars, this study assesses the current dust lifting schemes in the model, specifically the convective lifting and wind stress schemes. It is found that, by tuning lifting efficiency, the model with the convective lifting scheme can generally reproduce the seasonal variation of the mid-level atmospheric temperature (T15) but cannot reproduce the observed spatial distribution of dust devils, which exhibits non-homogeneous (uniform) distribution in the northern (southern) hemisphere. The model with the wind stress lifting scheme can generally capture the observed magnitude of T15 and column dust optical depth (CDOD) with properly tuned lifting efficiency and threshold drag velocity. There is a discrepancy in the assessment of modeling seasonal variations of dust with T15 and CDOD, which may be partly due to the observational uncertainties related to T15 and CDOD and the empirical modeling methods of Martian dust optical properties and radiative effect. For the spatial distribution of dust, there are significant simulation biases regardless of the tuning, which may be caused by the biases in the dust lifting process and large-scale atmospheric circulation. The analysis highlights that dust lifting schemes need further improvement to better represent the dust cycle and their impacts on Mars.

Plain Language Summary

Numerical models are important tools to study the dust cycle on Mars, but the ability of current numerical models to simulate the Martian atmospheric dust amount is still not very clear. Therefore, this study evaluates two dust lifting schemes in the widely used Martian model MarsWRF, i.e., the convective lifting scheme and wind stress lifting scheme. The model with the convective lifting scheme can reproduce the seasonal variation of the air temperature but cannot well reproduce the spatial distribution of convective processes that cause dust uplift. The model with the wind stress lifting scheme can capture the magnitude of air temperature and dust optical depth. However, there is a discrepancy in the assessment of simulated seasonal variation of dust with temperature and dust optical depth, which may be partly due to the observational uncertainties and the biases of modeling dust optical properties. There are also large modeling biases in the dust spatial distribution that may be related to the deficiency of the dust lifting process and large-scale atmospheric circulation around the polar region. The study brings some new perspectives on the assessment of dust lifting schemes and raises some problems to be solved.

1. Introduction

According to early observations (Capen & Martin, 1971; McKim, 1999), the yellow clouds observed by the telescope indicated the presence of dust in the Martian atmosphere. On Mars, dust is of significant importance to the Martian atmosphere, analogous to the importance of water to the Earth's atmosphere (Wu et al., 2022). The spatial and temporal distributions of dust are particularly important for the Martian atmosphere because dust in the atmosphere can interact with solar and infrared radiation (Haberle et al., 2017; Kahre et al., 2006; Pollack et al., 1990). The presence of airborne dust affects the atmospheric heating rate, which drives dynamic processes, so the presence of atmospheric dust strongly affects the circulation (Gierasch & Goody, 1968; Haberle et al., 1982).

According to the position of Mars to the sun (solar longitude, Ls), four seasons can be recognized on Mars: spring (Ls of 0–90°), summer (Ls of 90– 180°), autumn (Ls of 180–270°) and winter (Ls of 270– 360°). The general annual repeatability of the change in dust mass loading with the seasons constitutes the dust cycle in a year, which is characterized by the "non-dusty season" (Ls~0–135°) and the "dusty season" (Ls~135– 360°) (Kahre et al., 2017). "Non-dusty season" (Ls~0–135°) includes northern spring and early summer. During this season, the value of column dust opacity is relatively small except at high latitudes. According to the image data from Viking, MGS, MRO, and MEX, there is locally higher dust opacity near the edges of the seasonal CO_2 caps, caused by the enhanced winds related to topography and pressure variation that is related to the retreatment of two seasonal polar cap edges (Cantor et al., 2001; James et al., 1999). The "dusty season" (Ls~135– 360°) includes northern autumn and winter. Large-scale dust storms can often be observed during the "dusty season". During this time, dust storms on Mars were observed to exhibit various sizes and durations. Local dust storms (surface areas < $1.6 \times 10^6 km^2$ and lasting less than 2 sols) are the most frequently observed storms throughout the Martian year, mainly occurring near the edges of polar caps and the mid-latitude regions of both hemispheres (Cantor et al., 2002; 2010; 2001; Kahre et al., 2017; Toigo et al., 2018). Based on the image of Mars Global Surveyor MARS Orbiter Camera (MOC), regional dust storms (surface areas ≥ $1.6 \times 10^6 km^2$ and lasting more than 2 sols) occur about 8-35 times during Ls~130-160° and Ls~330-20° per year (Cantor, 2007; 2001). Most regional dust storms are caused by the merging of multiple local storms, loading more dust into the atmosphere and increasing the atmospheric temperature. Global-scale dust storms (GDSs), consisting of two to three regional dust storms, are the major atmospheric events lasting from several weeks to months

in the Martian atmosphere. According to observations by spacecraft and telescopes, most GDSs occur every 2 to 3 Martian years and cover almost all longitudes of both hemispheres (Basu et al., 2006; Bertrand et al., 2020; Viúdez‐Moreiras et al., 2019; Zurek & Martin, 1993).

Since Gierasch and Goody (1972) first showed that observed dust has a significant effect on the thermal state of the Martian atmosphere, numerical models have been used to study the Martian dust cycle. These models are developed following the models of the Earth. The mechanisms of dust injection into the Martian atmosphere are challenging for developing Martian GCMs. There have been many studies focusing on the parameterization of dust lifting in the model (Merrison et al., 2007; Newman & Richardson, 2015). Wilson & Hamilton (1996) implemented a dust injection scheme based on the heat and momentum exchange between the surface and the atmosphere. With the scheme, the model can successfully simulate the seasonal cycle of dust opacities compared to the observations from Mariner-9 and Viking, although global dust storms cannot be simulated. Later, Newman et al. (2002a, 2002b) developed a new set of active dust injection schemes, which can deepen the understanding of the dust life cycle and its impacts on the atmospheric state. The model with these schemes can also produce regional dust storms to some extent. Kahre et al. (2006) compared a modified Earth-based dust lifting mechanism (Westphal et al., 1987) for the Martian environment and the mechanism proposed by Newman et al. (2002b). They found that both can reproduce the dust cycle in a nonglobal dust storm year, as observed by TES.

So far, the two schemes proposed by Newman et al. (2002b) are most commonly used in the model for dust lifting. The first is the lifting of dust caused by surface wind stress, which only occurs when the surface stress is greater than an estimated threshold, including the saltation of sand (larger dust particles with diameters greater than 20 μm) and the suspension of smaller dust particles (diameter smaller than 20 μm) (Greeley & Iversen, 1987). Previous studies indicated that dust could be lifted by the saltation of sand particles when wind speeds on Mars are far below the wind stress of dust particles (Newman et al., 2002b; Pollack et al., 1976). Although sand particles are too heavy to remain aloft in the Martian atmosphere even if background vertical winds blow them up, the saltation of sand particles to the surface quickly increases the surface stress, which leads to dust particles being lifted more easily. The second is the lifting of dust by convective vortices (sometimes namely, dust devils), caused by the large pressure gradient and high tangential wind around the vortex core. Dust devils have been observed in the images taken by Viking Orbiter Cameras (Thomas &

Gierasch, 1985) and the MOC with different sizes and different durations Cantor et al., 2006; Fisher et al., 2005; Whelley & Greeley, 2006; 2008). They are mainly concentrated in the spring and summer seasons of the two hemispheres. Since the horizontal scales of the convective vortex are approximately a few centimeters to hundreds of meters and the vertical scale is up to the top of the convective boundary layer, the dust lifting process caused by the convective vortex occurs more easily than that caused by surface wind stress.

Understanding the effects of dust on the Martian atmosphere requires accurate spatial and temporal distributions of atmospheric dust. Previous studies showed that different combinations of dust lifting schemes could be adjusted to obtain reasonable dust opacity throughout a Martian year compared to the observations. Kahre et al. (2006), using the NASA Ames Mars GCM, suggested that the contributions from convective lifting and wind stress lifting were equal to the total dust mass loading in a Martian year without global dust storms. Whelley and Greeley (2008), based on the MOC images, suggested that the dust flux lifted by the convective process should be half of that lifted by near-surface wind stress. Newman et al. (2005) showed that the contribution of convective lifting was not as large as illustrated by previous studies, although they did not provide an exact ratio. Using different models and different environment settings, different relative contributions of the two lifting processes may be obtained.

So far, the contributions of the two dust lifting schemes are still uncertain because a few parameters related to the lifting efficiency and threshold in the schemes cannot be constrained with direct observations; instead, they are often tuned by indirect observations. For example, most previous studies adjusted these parameters mainly to produce a reasonable atmospheric temperature. Basu et al. (2004) simulated dust cycles over several Martian years without global dust storms. They were able to produce a global mean atmospheric temperature highly similar to the observations in spring and summer by adjusting the parameters in the two dust lifting schemes. However, the tuning parameters cannot be sufficiently constrained by atmospheric temperature alone. In addition, it is also necessary to evaluate the performance of individual lifting schemes and understand their deficiencies rather than evaluating the combined performance of the two lifting schemes. Therefore, in this study, two fields, atmospheric temperature and column dust optical depth (CDOD), are used together to provide a comprehensive assessment of the two dust lifting schemes in a Mars GCM. Both the temporal and spatial characteristics of the focused fields are examined. Section 2 introduces the MarsWRF GCM employed for this study. The design of the experiments and data used are also described. Section 3.1 evaluates the convective lifting scheme using

temperature and the spatial distribution of dust devils. Section 3.2 shows the evaluation of the wind stress lifting scheme from temporal and spatial distributions by using temperature and CDOD. The conclusion and discussion are shown in Section 4.

2. Methodology

2.1 Model and experiments

2.1.1 MarsWRF

MarsWRF is a three-dimensional (3-D) numerical model for the Martian atmosphere developed based on the Weather Research and Forecasting (WRF) mesoscale model for the Earth (Guzewich et al., 2013; Richardson et al., 2007; Toigo et al., 2012). Atmospheric processes can be examined by MarsWRF at various resolutions from the microscale to global-scale (Fenton & Richardson, 2001; Hinson & Wilson, 2002; Wu et al., 2021; Xiao et al., 2019).

The processes related to the dust life cycle in this model include dust lifting into the atmosphere, vertical mixing and diffusion, horizontal advection, and sedimentation. Dust lifted into the air can lead to radiative effect on the atmosphere at both solar and thermal infrared wavelengths. Therefore, a reasonable simulation of the spatial and temporal distributions of atmospheric dust is crucial to understanding the thermal and dynamic structures of the Martian atmosphere.

2.1.2 Dust scheme

To simulate the dust life cycle and its impact on the atmosphere, the dust lifting process from the surface into the atmosphere should be simulated properly. This study investigates two dust lifting schemes available in MarsWRF (Newman et al. (2002b): the convective lifting scheme (Section 2.1.2.1) and the near-surface wind stress lifting scheme (Section 2.1.2.2). The mechanisms of these two schemes, their formulation and the relevant tuning parameters are described below.

2.1.2.1 Convective Lifting

The convective lifting of dust results from atmospheric vortices that exist not only on Earth but also on Mars. Martian convective lifting of dust (dust devil) can be seen through Viking Orbiter Camera images (Thomas & Gierasch, 1985) and Mars Global Surveyor Mars Orbiter Camera images (Cantor et al., 2001). The low pressure in the center of the dust devil,

surrounded by strong tangential winds and a vertical upward velocity structure, can effectively suck in dust from the surface up to the top of the convective boundary layer. This process is generally small-scale, contributing to the small dust particles in the Martian atmosphere.

Rennó et al. (1998) developed a parameterization of the small-scale convective motion of dust based on thermodynamic theory, and Newman et al. (2002b) implemented it in MarsWRF. The convective lifting flux of dust is defined as

$$F_{CL} = \alpha_{CL} \cdot F_s \cdot \eta, \quad (1)$$

α_{CL} is a tunable efficiency parameter for convective lifting with units of $kg\ J^{-1}$, F_s is the sensible heat flux ($W\ m^{-2}$), and η is the thermodynamic efficiency, which is given by $1 - b$, where

$$b = \frac{p_s^{\chi+1} - p_{top}^{\chi+1}}{(p_s - p_{top})(\chi+1)p_s^{\chi}}, \quad (2)$$

where p_s is the surface pressure (Pa), p_{top} is the pressure at the top of the convective boundary layer (Pa), and χ is the specific gas constant divided by the specific heat capacity at constant pressure. According to Eq. 2, it can be seen that η increases with the height of the convective boundary layer.

In this convective lifting scheme, dust can be lifted as long as the upward heat flux at the surface is positive regardless of the dust particle size. At noon and afternoon, the solar radiation received by the surface increases, and consequently, the upward heat flux at the surface increases, which leads to an increase in the convective lifting flux.

2.1.2.2 Wind Stress Lifting

In addition to being lifted up by convective processes, dust can be blown into the atmosphere by near-surface wind stress. In the wind stress lifting scheme, a wind stress threshold is needed to determine the occurrence of dust events. In general, only very unfeasible high surface winds can lift dust particles at micron or smaller scales directly into the air (Bagnold, 1974). Instead, a steady movement of sand-sized particles (~100 μm) (i.e., saltation) can occur even under conditions with small wind speeds, increasing the near-surface wind stress by the saltating sand particles and lifting the surface dust. Therefore, the threshold at which the initial saltation can occur to make the sand move is the key to determining the wind stress lifting of dust. This threshold for sand-sized particle movement is calculated in MarsWRF as follows.

In the MarsWRF, the wind stress threshold τ_* ($\tau_* = \rho(u^t_{drag})^2$) is a function of the threshold drag velocity (u^t_{drag}). Dust can only be lifted when the actual drag velocity, u_{drag}, is greater than u^t_{drag}. The wind stress lifting scheme based on the saltation theory used in this study was formulated by White (1979). The magnitude of the vertical dust flux (F_{SL}) lifted from the surface is defined as

$$F_{SL} = \alpha_{SL} \cdot 2.61 \frac{\rho}{g} (u_{drag})^3 \left(1 - \frac{u^t_{drag}}{u_{drag}}\right)\left(1 + \frac{u^t_{drag}}{u_{drag}}\right)^2, \quad (3)$$

where α_{SL} is a tunable constant named the "lifting efficiency", ρ is the atmospheric density (kg m^{-3}), and g is the Martian gravity (m s^{-2}). The frictional wind speed in the atmospheric boundary layer proposed by Garratt (1994) is calculated as follows:

$$u_{drag} = \frac{ku(z)}{ln(\frac{z}{z_0})}, \quad (4)$$

where k is the von Karman constant, z is the height above the surface (m) and z_0 is the aerodynamic roughness length, taken as 0.01 m.

u^t_{drag} can be calculated by $\sqrt{\frac{\tau_*}{\rho}}$, with a constant τ_* or calculated with a semi-empirical formula:

$$u^t_{drag} = \beta \cdot A \sqrt{g D_P \frac{\rho_d}{\rho}}, \quad (5)$$

where D_P is the diameter of the dust (~4μm), ρ_d is the dust density of approximately 2500 kg m^{-3}, and A is a semi-empirical function of the friction Reynolds number that is defined as (using the formula in Newman et al. (2002b) here). Different surface roughness values will result in different friction Reynolds numbers and thus lead to different possibilities of dust lifting. The friction Reynolds number generally increases with the roughness of the surface. This study introduces a tunable coefficient β to account for the uncertainties of u^t_{drag}, and the default value is 1.0. More details about the formulas of wind stress lifting can be found in Newman et al. (2002a).

2.2 Numerical Experiments

All the experiments in this work are conducted at the global scale, where MarsWRF acts as a general circulation model (GCM). In this study, the global domain of MarsWRF has a horizontal spatial resolution of 5 degrees (36 latitude × 72 longitude grid points), with 52 vertical levels of non-uniform thickness located between the surface and the model top about 80 km in altitude. The model includes the treatment of topography derived from the Mars

Orbiter Laser Altimeter (MOLA); thermal inertia and albedo maps derived from Viking and Thermal Emission Spectrometer (TES) data; the CO_2 cycle, including the seasonal variations of the two polar ice caps; and the dust cycle and radiative interactions with dust and CO_2 in the visible and thermal infrared. None of the experiments in this work consider the presence of water vapor.

Sensitivity experiments of three parameters show that they can impact the dust lifting processes. The first one is lifting efficiency, α_{CL}, in the convective lifting scheme (Eq. 1). The other two free parameters can modulate the dust lifting flux in the wind stress lifting scheme (Eq. 3): lifting efficiency (α_{SL}) and threshold drag velocity (u^t_{drag}). In this study, u^t_{drag} is tuned by changing β. All the experiments conducted in this study are summarized in Table 1. The experiments of CL1, CL2, and CL3 are conducted by tuning the parameter α_{CL} in the convective lifting scheme to values of 1, 3, and 10 ($\times 10^{-9}\ kg\ J^{-1}$), respectively. For the wind stress lifting scheme, two parameters can be changed. To prevent them from affecting each other, in the experiments of SL1, SL2, and SL3, α_{SL} is set to the same value of $5\times 10^{-7}\ m^{-1}$ and β is changed to the values of 1, 0.35, and 0.1, respectively. Experiments with fixed β but changing α_{SL} are not conducted and discussed in this study, but the effect is similar. The values of α_{CL} and β are selected intentionally to cover all the probability of dust distribution that may occur. CAP and SL2 use the same settings except that the lifting efficiency in CAP is increased to $5\times 10^{-6}\ m^{-1}$ ($4\times 10^{-5}\ m^{-1}$) near the southern (northern) ice cap once CO_2 ice sublimation occurs in the past 30 sols. All experiments are run for one Martian year that does not include global-scale dust storms. The simulations are cycled for two years. The first year of simulation is treated as a spin-up, and the simulation results for the second year are analyzed.

2.3 Observation and reanalysis datasets

As mentioned above, the aim of this study is to improve our understanding of physical processes in the Martian dust cycle by re-evaluating the wind stress lifting scheme and convective lifting scheme using multiple observational datasets. In recent decades, Martian atmospheric conditions have been constantly detected by spacecraft and ground-based observations. The observations of Martian temperature and dust optical depth can be obtained. Montabone et al. (2015) obtained a multiannual climatology of the column dust optical depth dataset (referred to as the LMD dataset below) using observations of the Martian atmosphere from MY24 to MY34 by different orbiting instruments. The observations for eight Martian

years without global-scale dust storms represent the climatology of Martian dust and are used to evaluate the accuracy of the simulated dust cycle. In addition, the CDOD and temperature of the climatology scenario (with non-global dust storms) in the Mars Climate Database, version 5.3 (MCD v5.3), a database of meteorological fields derived from state-of-the-art Martian GCM numerical simulations and validated using available observational data, are also used(Forget et al., 1999; Madeleine et al., 2011).

3. Results

3.1 Convective lifting process

To examine the performance of the convective lifting scheme of dust, three experiments with the convective lifting process only are conducted by adjusting the sensitivity coefficient α_{CL} to modulate dust emission fluxes, and the specific adjustment of α_{CL} is shown in Table 1. According to the seasonal variation of zonal-mean dust lifting flux shown in Figure 1, α_{CL} increases gradually from CL1 to CL3, which corresponds to a rise in the amount of dust injected into the air, especially around $30^{\circ}N$ in spring and summer in the northern hemisphere, and around $30^{\circ}S$ in spring and summer in the southern hemisphere. The large value of dust lifting is near $30^{\circ}N$ ($30^{\circ}S$) in the spring and summer corresponding to both hemispheres, which is related to solar radiation. Because of the large eccentricity of Mars compared to the Earth, Mars is near the perihelion of the Sun during the spring and summer in the southern hemisphere, resulting in much more solar radiation being received during that period than during the aphelion of Mars.

In some previous studies (Basu et al., 2004; Newman & Richardson, 2015), the brightness temperature of the 15-μm channel derived from the Viking Orbiter IRTM is preferred to assess the realism of dust loading due to the dust radiative effect in the atmosphere**.** Therefore, T15 refers to the brightness temperature of the IRTM 15-μm channel or the temperature calculated from the corresponding IRTM 15-μm channel weighting function, which mainly reflects the temperature at altitudes of 10-40 km (centered at ~25 km or ~50 Pa) between the latitudes of $40^{\circ}S$ and $40^{\circ}N$. The use of T15 to evaluate the model is based on the assumption that when the simulated results are close to the observed air temperature, the simulated dust distribution is considered reasonable. Figure 2 shows the seasonal magnitude and variation of T15. In Figure 2a, the magnitude of T15 in the left panel shows that as α_{CL} increases, the increase of dust amount in the atmosphere leads to the strengthening of atmospheric warming. All three experiments reflect that T15 shows the

seasonal cycle of low temperature in boreal spring and summer and high temperature in autumn and winter. In the three experiments, the T15 in CL2 is the closest to that in MCD, especially in boreal spring and summer. This indicates that the temperature variation in boreal spring and summer can be well simulated using the convective lifting scheme only, and there is a slight underestimation for autumn. To better study the seasonal variation of temperature, the normalized T15 is calculated by dividing it by its maximum value in the year. As seen from the normalization of T15 in the right panel, the seasonal variation in T15 can be simulated using the convective lifting scheme alone, and the pattern of the seasonal variation is similar regardless of α_{CL}.

The dust devil is a vortex motion that causes dust uplift as the main contributor to convective lifting. The convective lifting scheme is developed based on the thermodynamic theory of dust devils to reproduce the background dust caused by this process. However, the comparison with observations reveals that there are still large caveats in this scheme. Cantor et al. (2006) showed that the dust devils observed by MOC are mainly concentrated in the latitude range from $71.9^{\circ}S$ to $62.2^{\circ}N$. They also showed the distribution characteristics of more dust devils in the northern hemisphere (about 88.5%) and less in the southern hemisphere. The distribution of dust devils in the northern hemisphere is uneven, with the majority of dust devils concentrated near Amazonis Planitia. The observed dust devils in the southern hemisphere are much less than those in the northern hemisphere, but the distribution is uniform.

The spatial distribution of the dust lifting flux caused by convective processes can be seen in Figure 3a. The simulated results with convective processes can generally reflect the spatial distribution of lifting dust associated with dust devils. The dust lifting fluxes are the largest in the northern Amazonis Planitia relative to other regions. In comparison, the distribution of dust lifting fluxes in the southern hemisphere is more uniform. Although the convective lifting fluxes show a similar spatial distribution as above, the lifting fluxes and the number of dust devils are significantly different. Therefore, this study also compares the simulated frequency of convective lifting with observations. When the convective lifting flux of dust is greater than zero, it is considered a dust devil event. The frequency of dust devils is obtained by accumulating the number of dust devils and dividing by the total number of days in a Martian year. If the frequency is closer to 1, it indicates that the dust devil has a greater probability of occurring, closer to the occurrence once a day, and on the other hand, it means no dust devil event occurred when the frequency is closer to 0. The spatial distribution of the

frequency of dust devils (Figure 3b) shows that the frequency of dust devils in the mid-latitudes of the two hemispheres is close to 1 and is reduced near the equator and high latitudes. The dust devils in the middle latitudes of the northern hemisphere are uneven, and there are three areas with a larger frequency of dust devils, while the distribution of dust devils in the southern hemisphere is more uniform. However, compared with the observation, there are two problems. First, the number of dust devils near Amazonis Planitia in the northern hemisphere observed by MOC is the largest (Cantor et al., 2006), but the three simulated areas of high values of dust devil occurrence do not include northern Amazonis Planitia. Second, there are more dust devils in the mid-latitudes in the southern hemisphere than in the northern hemisphere, which is also inconsistent with observations. The discussion above illustrates that although the model with the current convective lifting scheme can be tuned to capture the observed seasonal variation of global mean atmospheric temperature, it cannot reproduce the non-uniform spatial and temporal distribution of dust devils. This is mainly because dust devils can occur anywhere in the current model as long as there are processes of heat transport from the surface to the near-surface atmosphere, which deviates from the observed spatial distribution of the occurrence frequency of dust devils.

3.2 Wind stress lifting process

3.2.1 Seasonal variation

As discussed above, the convective lifting scheme has evident caveats, so can the model produce general features of the dust life cycle with the wind stress lifting scheme only and to what extent? This is focused on in the analysis below. Figure 4a shows the spatial distribution of the dust lifting flux caused by the near-surface wind stress lifting process. Only a few dust particles lifted in the northern hemisphere during autumn and winter, and almost no dust was lifted in other seasons. This is mainly because the threshold drag velocity (u_{drag}^{t}) prescribed in the model may be too high. Therefore, u_{drag}^{t} is reduced in the sensitivity experiments (as described above in Section 2.2), and the corresponding simulation results are shown in Figure 4b and Figure 4c. With decreasing u_{drag}^{t} from SL1 to SL3, the dust lifting is significantly enhanced, with total lifting masses of 2.85×10^{12}, 1.93×10^{14} and 4.87×10^{14} kg, respectively. In the spring and summer of the northern hemisphere (especially near $30^{\circ}N$) and that of the southern hemisphere (near $30^{\circ}S$), the dust mass lifted into the atmosphere increases. The two dust lifting centers (Ls=180° and Ls=0°) in the area near $30^{\circ}N$ become

more evident with the decrease of the threshold drag velocity. In addition, the uplift dust flux at the receding edge of the Antarctic ice cap has also increased significantly.

The change of u_{drag}^{t} affects the simulated dust concentration and thus changes the temperature in the Martian atmosphere. Figure 5 shows the seasonal variation of T15 simulated by these three experiences. It can be seen that the injected dust amount from SL1 to SL3 keeps increasing, leading to an improvement of the simulated T15 against the observation. Among the three experiments, T15 in SL2 is the closest to the observations, especially in boreal spring and summer, with a slight overestimation in boreal winter**.** The simulated T15 in SL3 is about 10 K higher than that in MCD throughout the year. SL1 significantly underestimates T15. After normalizing T15 (Fig. 5b), the seasonal variation in SL1 is small because a high threshold drag velocity prohibits dust lifting from the wind stress process throughout the year globally. Interestingly, the seasonal variation of the simulated T15 in SL3 is better than that in SL2, mainly reflected by the relative overestimation of T15 in boreal winter in SL2.

Previous studies suggested that it is necessary to combine convective lifting and wind stress lifting schemes to capture the temporal variation of T15. This is because the threshold drag velocity is set too large to lift dust through the wind stress process that is only allowed to occur in specific regions and seasons. To compensate for the underestimation of lifted dust from the wind stress process, previous studies applied the current convective scheme to capture the global mean atmospheric temperature. However, as discussed above, the current convective scheme cannot produce a reasonable spatial distribution of the observed occurrence of dust devils. According to Fig. 5, it is possible to reproduce the seasonal magnitude and variation of T15 using the wind stress lifting scheme only with tuned parameters.

In addition to T15, which is often used to assess the accuracy of Martian dust simulation, dust optical depth (DOD) is another important metric to assess simulated dust. However, most previous studies chose only one of the two for the evaluation (Basu et al., 2004; Kahre et al., 2006; Newman et al., 2002a). In this study, the assessments with both are compared. The seasonal magnitude and variation of the global average column integrated DOD (CDOD) are shown in Figure 6. According to the left panel, the observed CDOD shows consistent dust seasonal variation as reflected by T15, i.e., less dust in boreal spring and summer and more dust in boreal autumn and winter. In addition, there are two peaks in autumn and winter, with the main peak roughly between Ls = $200^{\circ} - 270^{\circ}$, where the observed CDOD can reach a

maximum of 0.3, and a weaker peak between Ls = $315^{\circ} - 340^{\circ}$. The CDOD in SL1 is very small throughout the year. After normalization, the seasonal variation of CDOD in SL1 can also be seen, but its value in spring and summer is significantly underestimated. The CDOD in SL2 is the closest to the observations among all three experiments in magnitude and variation, particularly in spring and summer. Consistent with that reflected by T15, SL3 overestimates CDOD throughout the year. In addition, it also relatively overestimates the CDOD in spring and summer, which is not in line with its performance on T15. All the experiments cannot capture the two peaks shown in the MCD reanalysis dataset. This may be partly due to that large dust particles are quickly settled down in the current model with only one dust particle size (Wang et al., 2021), which deserves further investigation.

According to the assessment with CDOD, the performance of SL2 seems to capture the observed seasonal magnitude and variation of global mean dust well and overwhelm the other two experiments. However, according to Fig. 5, SL2 seems to relatively overestimate T15 in boreal winter. One reason for the discrepancy may be due to the sampling inconsistency of T15 and CDOD in the dataset. As mentioned above, T15 reflects the temperature at altitudes of 10-40 km (centered at ~25 km or ~50 Pa) between the latitudes of $40^{\circ}S$ and $40^{\circ}N$, while CDOD reflects the global mean dust at all heights. The global average atmospheric temperature at altitudes of 10-40 km and altitudes of up to 80 km is shown in Figure S1 and Figure S2, respectively (in the supporting material). SL2 still relatively underestimates the temperature in spring and summer. Therefore, the inconsistency between the assessment of SL2 with T15 and CDOD cannot be attributed to sampling differences in T15 and CDOD. There may be two reasons for the inconsistency. One is the observational uncertainties related to T15 and CDOD, which may deserve further investigation about the retrieval or assimilation methods. Another reason may be the biases of modeling the optical properties of Martian dust, which is quite experimental in the current version of the model. The deficiency in modeling dust optical properties and their radiative impact may lead to inconsistencies between the assessment with T15 and CDOD.

3.2.2 Spatial variation

In addition to the seasonal variation, the spatial distribution of dust is also important. Therefore, the simulated spatial distributions of dust are evaluated below. As shown by the observed CDOD in Fig. 7a1, the dust amount increases significantly in the polar region of the northern hemisphere near the summer solstice and is higher than that at the middle and low

462 latitudes. This may be because CO_2 ice sublimates, and a strong temperature gradient is
463 formed in the ice cap-non-ice cap regions near the edge of the Arctic ice cap, which enhances
464 the wind speed. The probability of dust lifted from the surface into the air is strengthened in
465 this region (James et al., 1999). However, the meridional distribution of dust in SL2 during
466 the summer solstice shows more dust at the low and middle latitudes and less dust at the high
467 latitudes, which is significantly different from the observations. SL3 also has such a
468 deficiency. It is worth noting that, whether using the current convective lifting scheme or
469 wind stress lifting scheme or even combining these two lifting schemes, the model cannot
470 reproduce the relatively high CDOD during the solstice in the polar regions.
471 To further assess the simulated spatial distribution of Martian dust, Figure 8 shows the
472 zonally averaged CDOD for the four seasons. In terms of magnitude, SL1 underestimates
473 dust, SL3 overestimates dust globally throughout the year, while SL2 produces much better
474 results than the LMD dataset (Figure 8a1-a4). Consistent with what is shown in Fig. 7, in
475 boreal spring and summer, the dust amount at the polar of the northern hemisphere in SL2 is
476 less than that observed, while the dust amount at the low and middle latitudes of the northern
477 hemisphere in SL2 is more than observed. In boreal autumn and winter, the dust amount in
478 the polar region of the northern hemisphere is significantly overestimated in SL2, while the
479 dust amount in the polar region of the southern hemisphere is underestimated. In boreal
480 winter, SL2 overestimates the dust amount at low and middle latitudes in both hemispheres.
481 It is worth noting that although SL3 significantly overestimates the magnitude of CDOD
482 globally, it produces a meridional distribution of CDOD similar to that of SL2 after
483 normalization (Fig. 8b1-b4). However, SL1, with a much lower amount of dust lifted globally,
484 produces a relatively higher dust amount at high latitudes in all seasons (peak in the southern
485 polar region in boreal summer and in the northern polar region in other seasons), which
486 indicates that tuning the threshold drag velocity can affect not only the simulated global mean
487 magnitude but also the spatial distribution of dust.
488 To further understand the different spatial distributions of normalized dust amounts
489 among the three experiments, the spatial and temporal variations of the drag velocity, the
490 threshold drag velocity, and the drag velocity averaged only for the time and space when it is
491 larger than the threshold are shown in Figure 9. The main difference among the three
492 experiments comes from their difference in threshold drag velocity, which is tuned
493 intentionally as discussed above. There is also some small difference in drag velocity among
494 the three experiments due to the feedback of changing dust amount on meteorological fields.

The results show a large threshold drag velocity and small drag velocity in SL1 throughout the year (Fig. 9a1 and b1). The drag velocity is rarely larger than the threshold drag velocity in SL1, only at middle and high latitudes in boreal autumn and winter. This indicates that the normalized spatial variation in SL1 in summer (Fig. 8b2) is mainly due to the numerical calculation without any physical meaning. With the decrease of the threshold drag velocity in SL2 and SL3, the possibility of the drag velocity larger than the threshold drag velocity increases significantly, especially in the mid-latitudes in spring and summer of the two hemispheres, leading to the expansion of dust lifting areas and the increase of dust mass. The tuning of the threshold drag velocity can affect the spatial distribution of dust until it reaches a certain value with which the simulated normalized meridional distribution of dust tends to be similar.

In terms of the underestimation (overestimation) of dust amount at high latitudes (mid and low latitudes) in boreal spring and summer, part of the reason may be due to the underestimation of dust amount lifted at high latitudes (Fig. 4). The strong temperature gradient and hence the wind enhancement near the polar regions due to CO_2 ice sublimation may not be well simulated in the model (Chow et al., 2022; Kahre et al., 2006). In a sensitivity experiment (CAP), the wind stress lifting scheme is adjusted to increase the probability of dust lifting at the edge of the CO_2 ice cap as a function of the change of ice cap, and the bias of the spatial distribution of dust in boreal summer still cannot be reduced (Fig. S3 in the supporting material). Further analysis of the spatial patterns of dust emissions and mass loading (not shown) indicates that the bias may be related to biases not only in the dust lifting scheme in boreal summer but also in the simulated circulation and dust transport. The comparison of near-surface pressure and wind field between the simulations and the MCD dataset is shown in Figure 10. In boreal summer, the spatial distribution of the wind field and pressure in SL2 is quite different from that in the MCD dataset. The high-pressure center and the corresponding clockwise wind circulation around the polar region in SL2 are opposite to the low-pressure center and thus the counterclockwise wind rotation in the MCD dataset. It is worth noting that even though there is more dust mass lifted at high latitudes in the sensitivity experiment CAP, the spatial pattern of wind fields and pressure in CAP is similar to that in SL2, which may be related to the numerical filtering in MarsWRF to deal with the decreasing zonal grid at high latitudes (Toigo et al., 2012), which deserves further investigation.

4. Summary and discussion

The dust cycle plays an important role in the Martian atmosphere, and dust lifting is the first step in the dust cycle processes by lifting surface dust into the air. Therefore, this study focuses on the dust lifting schemes in the MarsWRF GCM. This model provides two widely used dust lifting schemes: a convective lifting scheme and a wind stress lifting scheme. Since the contributions of the two schemes are still uncertain, the ability of each scheme to simulate the dust cycle is discussed, focusing on the seasonal magnitude and variation of Martian dust.

For the convective lifting scheme, this study focuses on the simulations of the dust cycle by varying the lifting efficiency and assessing the simulations with the seasonal variation of T15 and the frequency of dust devils. Compared with T15, the convective lifting scheme can reproduce the seasonal variation of atmospheric temperature affected by dust regardless of the change in lifting efficiency. The magnitude of T15 in CL2 is closer to the observation data in the three experiments. This means that on Mars, the seasonal variation of global mean Martian dust can be reproduced by applying the convective lifting scheme alone. However, there are several problems with the simulated spatial distribution of dust devils compared with the frequency of observed dust devils. First, this scheme simulates fewer dust devils in northern Amazonis Planitia and cannot reproduce the phenomenon that the Martian dust devil reaches its peak in this region. Second, there are fewer dust devils in the mid-latitudes of the northern hemisphere and more dust devils in the southern hemisphere against the observations. This suggests that the current convective lifting scheme is not appropriate for simulating Martian dust, at least not based on sound physical mechanisms.

For the wind stress lifting scheme, this study focuses on simulations of the seasonal magnitude and variation of dust by varying the threshold drag velocity. To evaluate the dust lifting scheme more comprehensively, this study uses two metrics, T15 and CDOD, reflecting atmospheric temperature and dust optical depth, respectively. SL2 with appropriately tuned lifting efficiency and threshold dray velocity simulates the best magnitude of T15 against the reanalysis data but overestimates the seasonal variation due to its positive bias of T15 magnitude in boreal winter. However, SL2 can reproduce the seasonal magnitude and variation of CDOD well against the reanalysis. This discrepancy in the assessment with T15 and CDOD may be partly due to the observational uncertainties related to T15 and CDOD and the biases of experimentally modeling the optical properties and radiative feedback of Martian dust in the current model, which deserves further investigation. Overall, it is possible to reproduce the seasonal magnitude and variation of global mean atmospheric temperature and CDOD using the wind stress lifting scheme only with appropriately tuned parameters,

except that the model still cannot capture the observed bimodal structure in boreal autumn and winter, which needs to be improved in the future.

For the spatial distribution of dust simulated with the wind stress lifting process, the SL2 and SL3 experiments can generally simulate the meridional distribution of dust mass that decreases from the low to high latitudes. Although SL2 can generally capture the seasonal magnitude and variation of global mean dust amount, there are still significant biases in its simulated spatial distribution of dust no matter how parameters are tuned, such as it overestimates dust amount at low and middle latitudes in both hemispheres in boreal winter. In addition, the simulations cannot capture the observed relatively high dust mass at high latitudes than at low and middle latitudes (boreal summer for the northern hemisphere and boreal winter for the southern hemisphere) that may be due to local dust storms occurring frequently at the cap edges of CO_2 ice in both hemispheres. The sensitivity experiments and analysis indicate that the biases in large-scale atmospheric circulation, particularly at high latitudes, may also contribute to the underestimation of dust over polar regions. Please note that these modeling biases in spatial distribution cannot be mitigated with the combination of current convective lifting and wind stress lifting schemes. The results also indicate that tuning the threshold drag velocity can affect not only the simulated global mean magnitude but also the spatial distribution of dust.

There are some limitations in the assessment of this study. This study focuses on the impact of the dust lifting process on the spatial and temporal distributions of atmospheric dust, ignoring to discuss many other processes that affect dust distributions, such as sedimentation, PBL mixing, sublimation of the CO_2 ice cap, and dust radiative feedback. In addition, only one size of dust particle is used in the simulations. The influence of dust particles simulated with more sizes needs to be assessed in the future. Due to the availability of observations, this study uses only two metrics, T15 and CDOD, to evaluate the dust lifting schemes. Directly observed or retrieved dust lifting fluxes and vertical distributions of dust properties would be very helpful for further understanding the Martian dust cycle and improving Martian dust modeling.

Data Availability Statement

The reconstructed column dust optical depth based on Montabone et al. (2015) are freely download at http://www-mars.lmd.jussieu.fr/mars/dust_climatology/index.html. The Mars Climate Database outputs used in this study can be obtained from

https://doi.org/10.5281/zenodo.7437175. The MarsWRF model outputs are available at https://doi.org/10.5281/zenodo.7437972.

Author contributions

Lulu Li and Chun Zhao designed the experiments and conducted and analyzed the simulations. All authors contributed to the discussion and final version of the paper.

Acknowledgments

This research was supported by the Strategic Priority Research Program of Chinese Academy of Sciences (grant XDB41000000), the National Key Research and Development Program of China (2016YFA0602001), the National Natural Science Foundation of China (42061134009, 41775146), the Fundamental Research Funds for the Central Universities, the USTC Research Funds of the Double First-Class Initiative, and the study used the computing resources from the High-Performance Computing Center of University of Science and Technology of China (USTC) and the TH-2 of National Supercomputer Center in Guangzhou (NSCC-GZ).

References

Bagnold, R. A. (1974). The Physics of Blown Sand and Desert. *Methuen, New York*.

Basu, S., Richardson, M. I., & Wilson, R. J. (2004). Simulation of the Martian dust cycle with the GFDL Mars GCM. *Journal of Geophysical Research: Planets, 109*(E11).

Basu, S., Wilson, J., Richardson, M., & Ingersoll, A. (2006). Simulation of spontaneous and variable global dust storms with the GFDL Mars GCM. *Journal of Geophysical Research, 111*(E9).

Bertrand, T., Wilson, R. J., Kahre, M. A., Urata, R., & Kling, A. (2020). Simulation of the 2018 global dust storm on Mars using the NASA Ames Mars GCM: a multitracer approach. *Journal of Geophysical Research: Planets, 125*(7), e2019JE006122.

Cantor, B., Malin, M., & Edgett, K. S. (2002). Multiyear Mars Orbiter Camera (MOC) observations of repeated Martian weather phenomena during the northern summer season. *Journal of Geophysical Research: Planets, 107*(E3), 3-1-3-8.

Cantor, B. A. (2007). MOC observations of the 2001 Mars planet-encircling dust storm. *Icarus, 186*(1), 60-96.

Cantor, B. A., James, P. B., & Calvin, W. M. (2010). MARCI and MOC observations of the atmosphere and surface cap in the north polar region of Mars. *Icarus, 208*(1), 61-81.

Cantor, B. A., James, P. B., Caplinger, M., & Wolff, M. J. (2001). Martian dust storms: 1999 Mars orbiter camera observations. *Journal of Geophysical Research: Planets, 106*(E10), 23653-23687.

Cantor, B. A., Kanak, K. M., & Edgett, K. S. (2006). Mars Orbiter Camera observations of Martian dust devils and their tracks (September 1997 to January 2006) and evaluation of theoretical vortex models. *Journal of Geophysical Research: Planets, 111*(E12), n/a-n/a.

Capen, C. F., & Martin, L. J. (1971). The developing stages of the Martian yellow storm of 1971. *Lowell Observatory Bulletin, 7*, 211-216.

Chow, K.-C., Xiao, J., & Wang, Y.-M. (2022). Simulation of dust activities in the southern high latitudes of Mars. *Planetary and Space Science, 217*.

Fenton, L. K., & Richardson, M. I. (2001). Martian surface winds: Insensitivity to orbital changes and implications for aeolian processes. *Journal of Geophysical Research: Planets, 106*(E12), 32885-32902.

Fisher, J. A., Richardson, M. I., Newman, C. E., Szwast, M. A., Graf, C., Basu, S., et al. (2005). A survey of Martian dust devil activity using Mars Global Surveyor Mars Orbiter Camera images. *Journal of Geophysical Research: Planets, 110*(E3).

Forget, F., Hourdin, F., Fournier, R., Hourdin, C., Talagrand, O., Collins, M., et al. (1999). Improved general circulation models of the Martian atmosphere from the surface to above 80 km. *Journal of Geophysical Research: Planets, 104*(E10), 24155-24175.

Garratt, J. R. (1994). THE ATMOSPHERIC BOUNDARY-LAYER - REVIEW. *Earth-Science Reviews, 37*(1-2), 89-134. <Go to ISI>://WOS:A1994PN31900002

Gierasch, P., & Goody, R. (1968). A study of the thermal and dynamical structure of the Martian lower atmosphere. *Planetary and Space Science, 16*(5), 615-646.

Gierasch, P., & Goody, R. (1972). The effect of dust on the temperature of the Martian atmosphere. *Journal of the Atmospheric Sciences, 29*(2), 400-402.

Greeley, R., & Iversen, J. D. (1987). *Wind as a geological process: on Earth, Mars, Venus and Titan*: CUP Archive.

Guzewich, S. D., Toigo, A. D., Richardson, M. I., Newman, C. E., Talaat, E. R., Waugh, D. W., & McConnochie, T. H. (2013). The impact of a realistic vertical dust distribution on the simulation of the Martian General Circulation. *Journal of Geophysical Research: Planets, 118*(5), 980-993.

Haberle, R. M., Clancy, R. T., Forget, F., Smith, M. D., & Zurek, R. W. (2017). *The atmosphere and climate of Mars*: Cambridge University Press.

Haberle, R. M., Leovy, C. B., & Pollack, J. B. (1982). Some effects of global dust storms on the atmospheric circulation of Mars. *Icarus, 50*(2-3), 322-367.

Hinson, D., & Wilson, R. (2002). Transient eddies in the southern hemisphere of Mars. *Geophysical Research Letters, 29*(7), 58-51-58-54.

James, P. B., Hollingsworth, J. L., Wolff, M. J., & Lee, S. W. (1999). North polar dust storms in early spring on Mars. *Icarus, 138*(1), 64-73.

Kahre, M. A., Murphy, J. R., & Haberle, R. M. (2006). Modeling the Martian dust cycle and surface dust reservoirs with the NASA Ames general circulation model. *Journal of Geophysical Research-Planets, 111*(E6). <Go to ISI>://WOS:000238572200001

Kahre, M. A., Murphy, J. R., Newman, C. E., Wilson, R. J., Cantor, B. A., Lemmon, M. T., et al. (2017). The Mars Dust Cycle. In *The Atmosphere and Climate of Mars* (pp. 295-337).

Madeleine, J. B., Forget, F., Millour, E., Montabone, L., & Wolff, M. J. (2011). Revisiting the radiative impact of dust on Mars using the LMD Global Climate Model. *Journal of Geophysical Research-Planets, 116*. <Go to ISI>://WOS:000297419600003

McKim, R. (1999). Meeting contribution: recent views of Mars. *Journal of the British Astronomical Association, 109*, 287.

Merrison, J., Gunnlaugsson, H., Nørnberg, P., Jensen, A., & Rasmussen, K. (2007). Determination of the wind induced detachment threshold for granular material on Mars using wind tunnel simulations. *Icarus, 191*(2), 568-580.

Montabone, L., Forget, F., Millour, E., Wilson, R. J., Lewis, S. R., Cantor, B., et al. (2015). Eight-year climatology of dust optical depth on Mars. *Icarus, 251*, 65-95.

Newman, C. E., Lewis, S. R., & Read, P. L. (2005). The atmospheric circulation and dust activity in different orbital epochs on Mars. *Icarus, 174*(1), 135-160.

Newman, C. E., Lewis, S. R., Read, P. L., & Forget, F. (2002a). Modeling the Martian dust cycle 2. Multiannual radiatively active dust transport simulations. *Journal of Geophysical Research: Planets, 107*(E12), 7-1-7-15.

Newman, C. E., Lewis, S. R., Read, P. L., & Forget, F. (2002b). Modeling the Martian dust cycle, 1. Representations of dust transport processes. *Journal of Geophysical Research: Planets, 107*(E12), 6-1-6-18.

Newman, C. E., & Richardson, M. I. (2015). The impact of surface dust source exhaustion on the martian dust cycle, dust storms and interannual variability, as simulated by the MarsWRF General Circulation Model. *Icarus, 257*, 47-87.

Pollack, J. B., Haberle, R., Greeley, R., & Iversen, J. (1976). Estimates of the wind speeds required for particle motion on Mars. *Icarus, 29*(3), 395-417.

Pollack, J. B., Haberle, R. M., Schaeffer, J., & Lee, H. (1990). Simulations of the general circulation of the Martian atmosphere: 1. Polar processes. *Journal of Geophysical Research: Solid Earth, 95*(B2), 1447-1473.

Rennó, N. O., Burkett, M. L., & Larkin, M. P. (1998). A simple thermodynamical theory for dust devils. *Journal of Atmospheric Sciences, 55*(21), 3244-3252.

Richardson, M. I., Toigo, A. D., & Newman, C. E. (2007). PlanetWRF: A general purpose, local to global numerical model for planetary atmospheric and climate dynamics. *Journal*

of Geophysical Research: Planets, 112(E9). https://agupubs.onlinelibrary.wiley.com/doi/abs/10.1029/2006JE002825

Thomas, P., & Gierasch, P. J. (1985). Dust devils on Mars. *Science, 230*(4722), 175-177.

Toigo, A. D., Lee, C., Newman, C. E., & Richardson, M. I. (2012). The impact of resolution on the dynamics of the martian global atmosphere: Varying resolution studies with the MarsWRF GCM. *Icarus, 221*(1), 276-288.

Toigo, A. D., Richardson, M. I., Wang, H., Guzewich, S. D., & Newman, C. E. (2018). The cascade from local to global dust storms on Mars: Temporal and spatial thresholds on thermal and dynamical feedback. *Icarus, 302*, 514-536.

Viúdez‐Moreiras, D., Newman, C., De la Torre, M., Martínez, G., Guzewich, S., Lemmon, M., et al. (2019). Effects of the MY34/2018 global dust storm as measured by MSL REMS in Gale Crater. *Journal of Geophysical Research: Planets, 124*(7), 1899-1912.

Wang, Y., Chow, K.-C., Xiao, J., & Wong, C.-F. (2021). Effect of dust particle size on the climate of Mars. *Planetary and Space Science, 208*.

Westphal, D. L., Toon, O. B., & Carlson, T. N. (1987). A two‐dimensional numerical investigation of the dynamics and microphysics of Saharan dust storms. *Journal of Geophysical Research: Atmospheres, 92*(D3), 3027-3049.

Whelley, P. L., & Greeley, R. (2006). Latitudinal dependency in dust devil activity on Mars. *Journal of Geophysical Research, 111*(E10).

Whelley, P. L., & Greeley, R. (2008). The distribution of dust devil activity on Mars. *Journal of Geophysical Research: Planets, 113*(E7).

White, B. R. (1979). Soil transport by winds on Mars. *Journal of Geophysical Research: Solid Earth, 84*(B9), 4643-4651.

Wu, Z., Li, T., Heavens, N. G., Newman, C. E., Richardson, M. I., Yang, C., et al. (2022). Earth-like thermal and dynamical coupling processes in the Martian climate system. *Earth-Science Reviews, 229*.

Wu, Z., Richardson, M. I., Zhang, X., Cui, J., Heavens, N. G., Lee, C., et al. (2021). Large Eddy Simulations of the Dusty Martian Convective Boundary Layer With MarsWRF. *Journal of Geophysical Research: Planets, 126*(9).

Xiao, J., Chow, K.-C., & Chan, K.-l. (2019). Dynamical processes of dust lifting in the northern mid-latitude region of Mars during the dust storm season. *Icarus, 317*, 94-103.

Zurek, R. W., & Martin, L. J. (1993). Interannual variability of planet‐encircling dust storms on Mars. *Journal of Geophysical Research: Planets, 98*(E2), 3247-3259.

Table 1. Numerical experiments in this study.

Experiment	α_{CL} $(10^{-9}\ kg\ J^{-1})$	α_{SL} $(10^{-7}\ m^{-1})$	β	Cap affect
CL1	1	-	-	-
CL2	3	-	-	-
CL3	10	-	-	-
SL1	-	5	1	-
SL2	-	5	0.35	-
SL3	-	5	0.1	-
CAP	-	5	0.35	increase

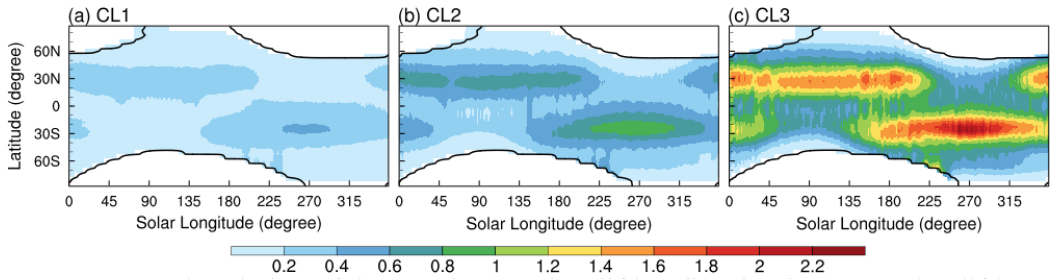

Figure 1. Seasonal variation of the zonal-mean dust lifting flux for the convective lifting scheme (shaded, $10^{-7} kg/m^2/s$). (a) CL1; (b) CL2; (c) CL3. The black contours depict the edges of CO_2 ice cap.

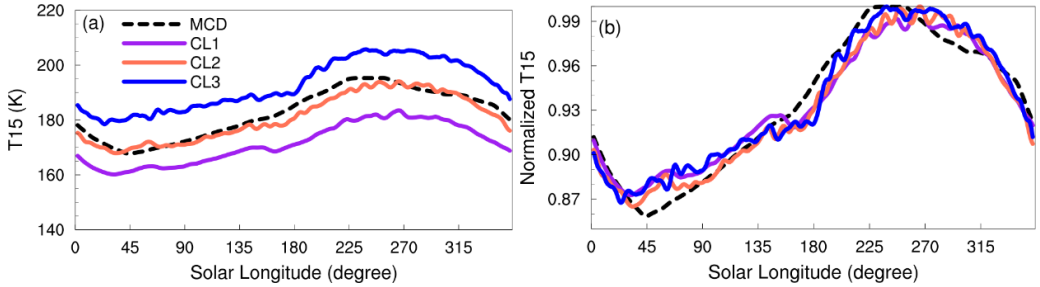

Figure 2. The seasonal variation of (a) the mid-level layer atmospheric temperature (T15) between $40^{\circ}S$ and $40^{\circ}N$ (in units of K); (b) normalized T15. The dashed line indicates the T15 in MCD, and the solid lines indicate the MarsWRF model simulation. The purple line is simulation CL1, the orange line is simulation CL2, and the blue line is simulation CL3.

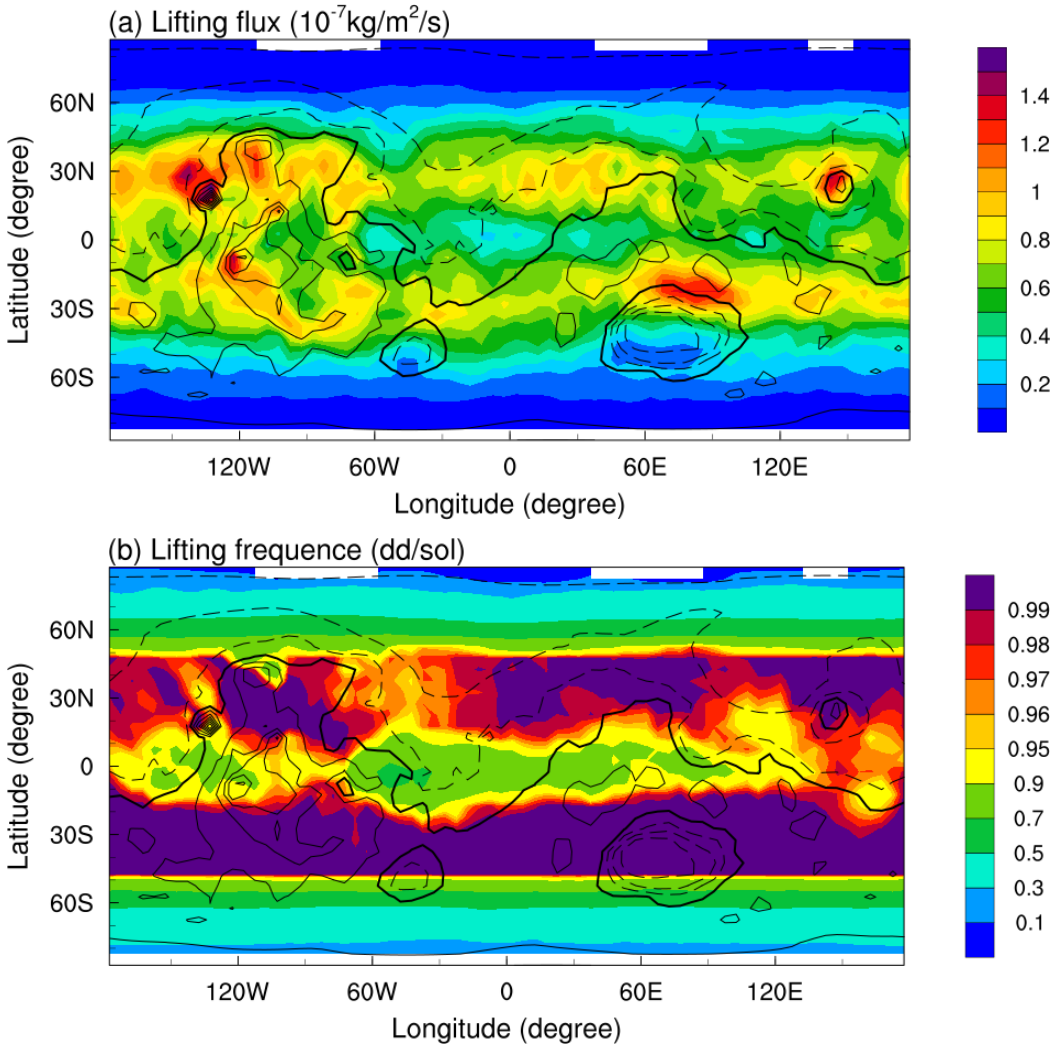

Figure 3. Spatial distribution of convective lifting averaged over the year at 14 pm. (a) Dust lifting flux (shaded, $10^{-7}kg/m^2/s$); (b) lifting frequency (dd/sol), equivalent to the occurrence frequency of dust devils in the model; contour lines indicate terrain height at 2 km intervals, solid lines are positive, dashed lines are negative.

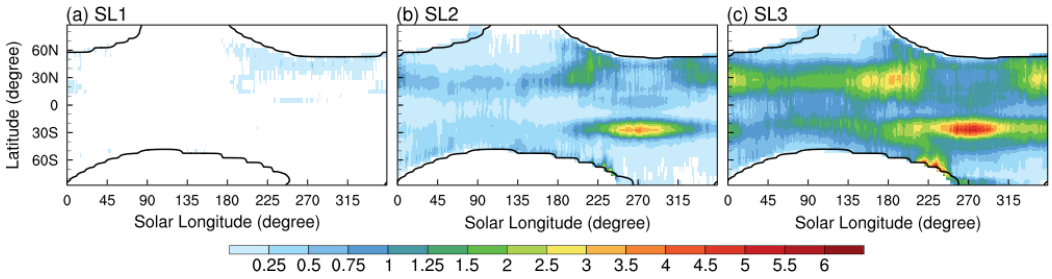

Figure 4. Same as Figure 1 but for the dust lifting flux (in units of $10^{-7} kg/m^2/s$) from the wind stress lifting scheme.

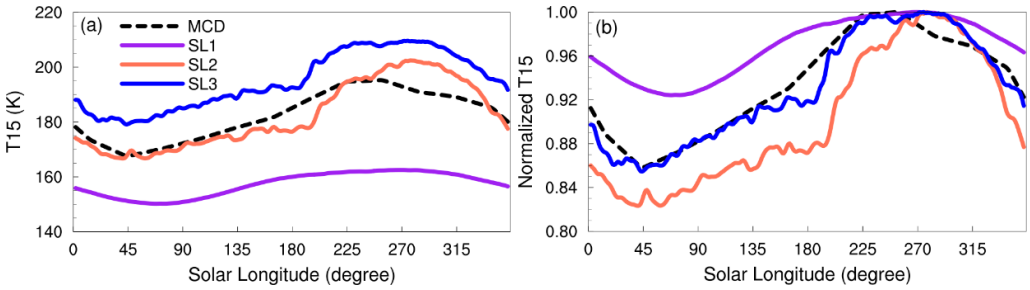

Figure 5. Same as Figure 2 but for the wind stress lifting scheme.

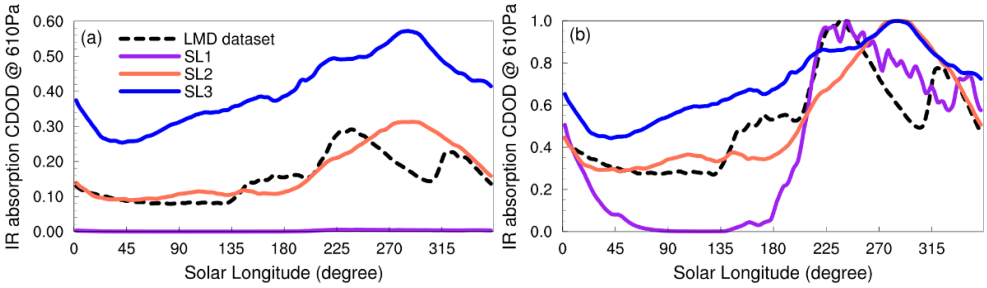

Figure 6. Temporal distribution of (a) the global average column dust optical depth in the infrared band at 610 Pa; (b) normalized IR absorption CDOD at 610 Pa. The dashed line indicates observations, and the solid lines indicate the MarsWRF model simulation. The black dashed line shows the reconstructed observation data of CDOD averaged for eight years from 24 to 34 excluding MY25, MY28 and MY34 when containing global dust storms (Montabone et al., 2015). The purple line is simulation SL1, the orange line is simulation SL2, and the blue line is simulation SL3.

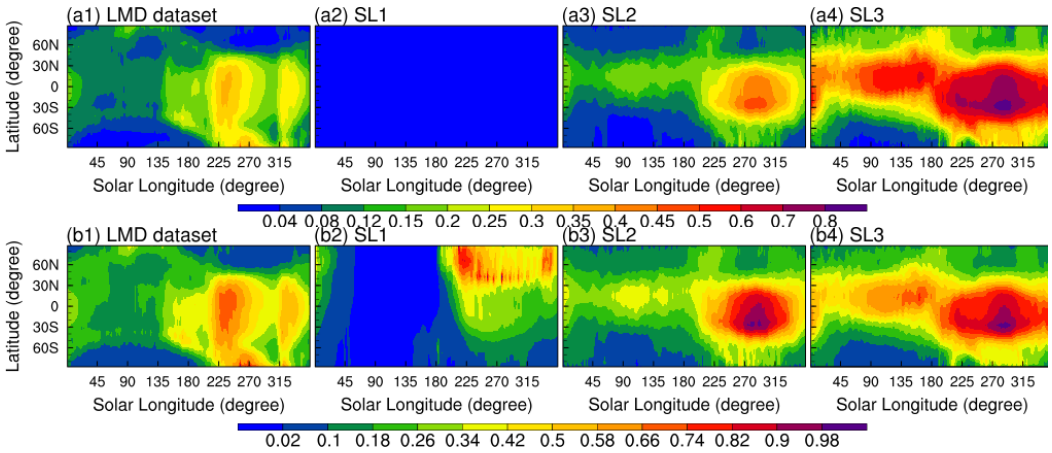

Figure 7. Seasonal variation of zonal-mean IR absorption CDOD at 610 Pa (shaded, upper panel) and normalized CDOD (shaded, lower panel). From left to right are the LMD data excluding three years with global dust storms, SL1, SL2 and SL3.

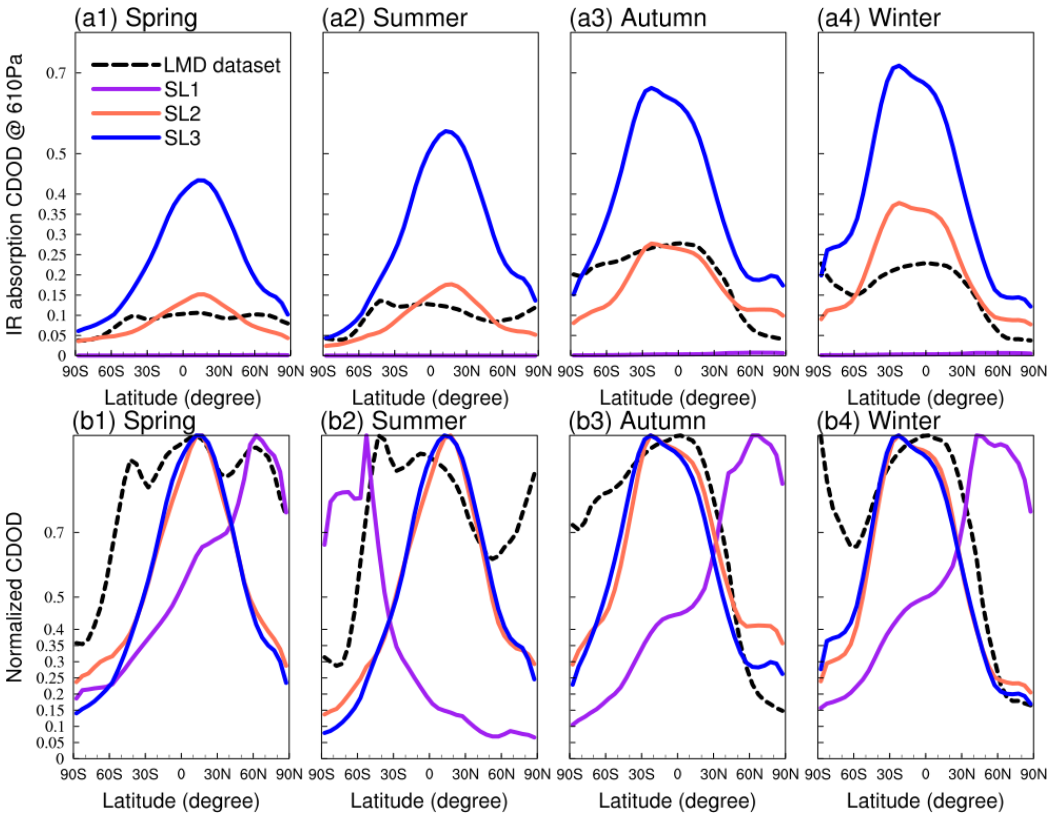

Figure 8. Zonally averaged CDOD for the four seasons (a1-a4) and normalized (b1-b4). Numbers from 1 to 4 correspond to spring, summer, autumn and winter. LMD dataset (dashed line), SL1 (purple), SL2 (orange), SL3 (blue).

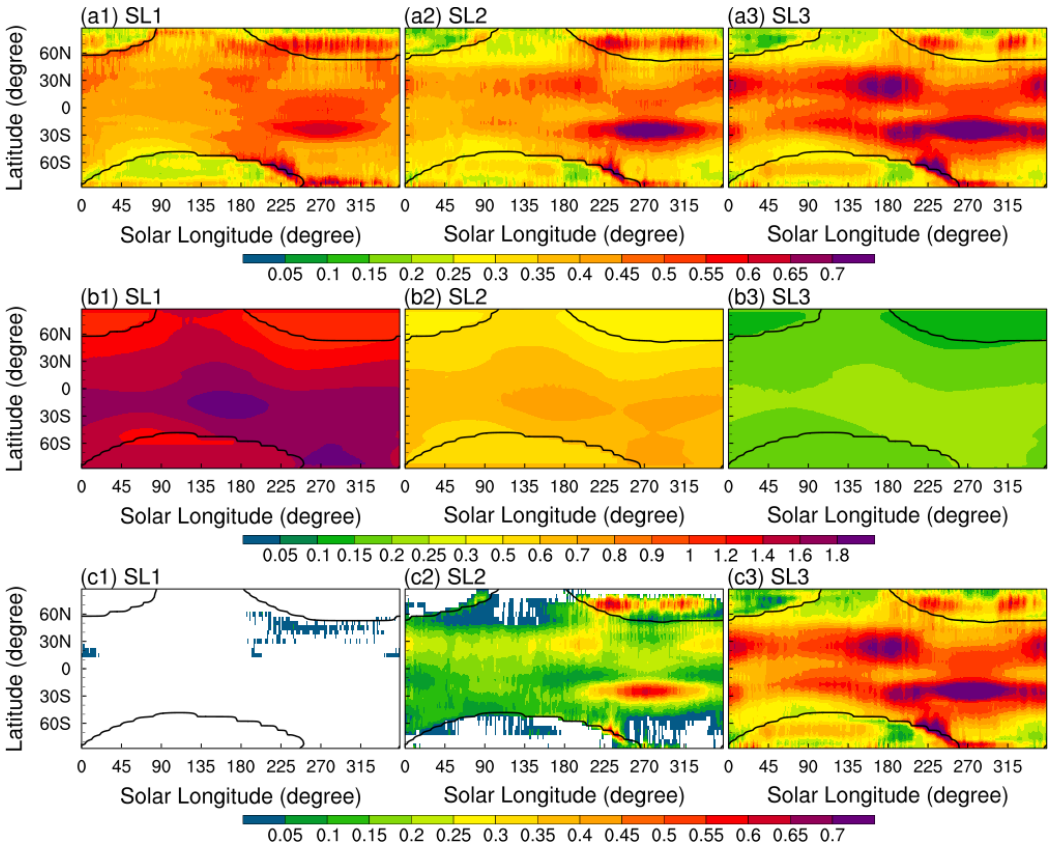

Figure 9. Seasonal variation of the drag velocity (shaded, top panel), the threshold drag velocity (shaded, middle panel) and the drag velocity averaged for the time and space when it is larger than the threshold drag velocity (shaded, bottom panel), in units of m/s. From left to right are SL1, SL2 and SL3. The black contours depict the edge of the CO2 ice cap.

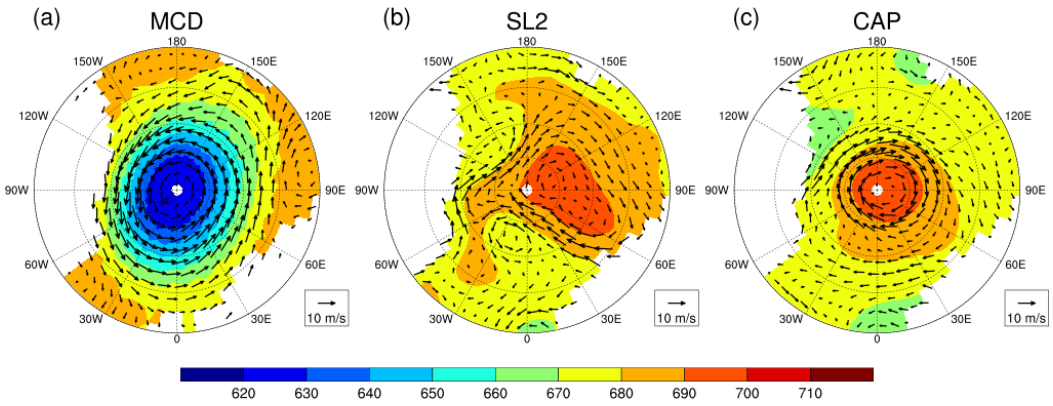

Figure 10. The pressure (shaded, in units of Pa) and wind field (vectors, in units of m/s) near the surface in the polar projection of the northern hemisphere at Ls = 90°; the outermost circle is $30^{\circ}N$. From left to right are the MCD, SL2 and CAP.